Bulletin of the New Zealand Society for Earthquake Engineering, Vol. 56, No. 3, September 2023

NUMERICAL MODELLING APPROACHES FOR PREDICTING THE SEISMIC RESPONSE OF MONOPILE-SUPPORTED DISSIPATIVE CONTROLLED ROCKING BRIDGE PIERS

Sabina Piras[1], Alessandro Palermo[2] and Gabriele Chiaro[3]

(Submitted *February 2022*; Reviewed *May 2022*; Accepted *December 2022*)

ABSTRACT

In this paper, rotational spring and multi-spring models are implemented in SAP2000® software, and numerical solutions are presented for monotonic and cyclic behaviour of a dissipative controlled rocking (DCR) bridge column supported on a monopile foundation that is embedded in sand. The pile-soil system is modelled with elastic frame elements connected to vertically-spaced bi-linear soil springs. Three soil conditions (i.e. loose, medium-dense and dense sand) are considered to account for soil-structure interaction effects. The results from an experimental programme, carried out by the authors at the University of Canterbury, are used to validate the numerical solutions. The numerical simulation results for the three sand conditions are in good agreement with the experimental ones. From a computational standpoint, the relatively simple mathematical formulation and easy implementation would make the rotational spring model more desirable than the complex multi-spring model. On the other hand, the multi-spring model is more versatile and capable of describing the cyclic response of the DCR pier, such as the post-tensioning force, axial stress in the steel dissipaters and gap-opening interface rocking characteristics.

https://doi.org/10.5459/bnzsee.1591

INTRODUCTION

Dissipative controlled rocking (DCR) connections, otherwise known as hybrid jointed ductile connections [1] or Hybrid PRESSS systems [2], are low-damage, ductile connections intended to eliminate the formation of plastic hinges in the substructure. When applied to bridge columns, DCR connections provide a self-centring capability through unbonded post-tensioning tendons and seismic energy dissipation through damping systems. The total moment capacity of the DCR joint is the sum of the moment contributions from the unbonded post-tensioning, axial load and the energy dissipaters.

Currently, there are three primary methods to numerically model DCR structures: section analysis method, rotational spring method, and multi-spring element modelling (Figure 1). An additional modelling technique would be finite element modelling (FEM); however, its use is still limited because it is more complex to implement, and its calibration requires detailed laboratory tests. FIB [3] presents a state-of-art of the various modelling approaches for post-tensioned rocking structures.

The procedure for calculating the moment-rotation response of a DCR connection using section analysis was first developed by Pampanin et al. [4] for concrete applications. The accurate representation of the contact rocking interface is a key challenge when modelling DCR connections because as rocking occurs, it results in a gap opening, and classical section analysis methods based on stress-strain are no longer applicable. An analogy with an equivalent cast-in-place connection named "Monolithic Beam Analogy" (MBA) was proposed by Pampanin et al. [4], which provides an additional condition related to the global member behaviour (displacement) necessary to develop a complete moment-rotation curve of the section. MBA was revisited by Palermo et al. [5] who established the revised Monolithic Beam Analogy (rMBA), which recognises that the post-tensioned system is inherently more flexible than the equivalent monolithic element. Further details regarding the rMBA method can be found in Palermo et al. [5].

A rotational spring model uses bi-linear or tri-linear rotational springs to model the moment-rotation response of elements in a DCR system. Two "zero-length" rotational springs are placed in parallel to model the response of the unbonded post-tensioning and dissipaters at the rocking surface [6].

A multi-spring element modelling approach provides more computation accuracy than the rotational spring modelling method [7]. The multi-spring model is a macro model that consists of compression-only axial springs located at the rocking interface, simple bi-linear springs to model the steel dissipaters, a post-tensioned self-centring bar, and elastic frame elements for the column.

One of the key objectives of this research is to investigate experimentally and numerically the influence of soil-structure interaction (SSI) on the seismic response of DCR columns. Following the experimental testing activity described in Piras et al. [8], a rotational spring model and multi-spring model are adopted to predict the seismic performance of a DCR bridge column supported on a monopile foundation with the influence of SSI. For most typical structures, accommodating SSI in a structural analysis will reduce the computed design base shears due to period lengthening [9]. SSI is a very complex problem to model; however, indirect modelling approaches have been developed whereby the properties of the underlying soils are derived and idealised in a simplified representation as springs. For pile foundations, or monopiles, the SSI is often time idealised using either an uncoupled spring model, or p-y (horizontal) and t-z (vertical) soil springs (Figure 2) [9].

[1] *Corresponding Author, PhD Candidate, University of Canterbury, Christchurch, sabpiras@gmail.com (Member)*
[2] *Professor, University of Canterbury, Christchurch, alessandro.palermo@canterbury.ac.nz (Fellow)*
[3] *Associate Professor, University of Canterbury, Christchurch, gabriele.chiaro@canterbury.ac.nz (Member)*

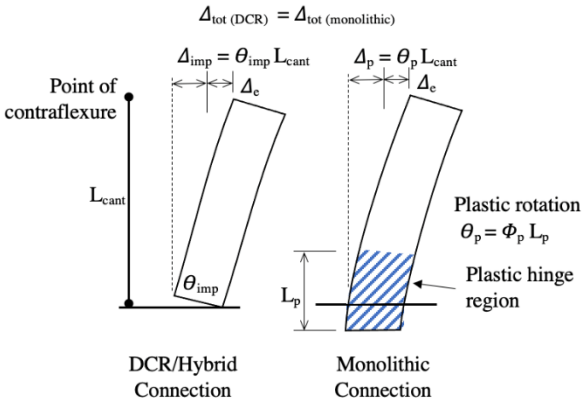

(a) Section analysis using the Monolithic Beam Analogy (MBA) method

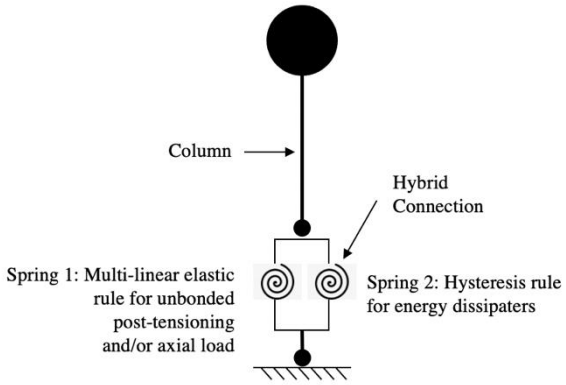

(b) Rotational spring model

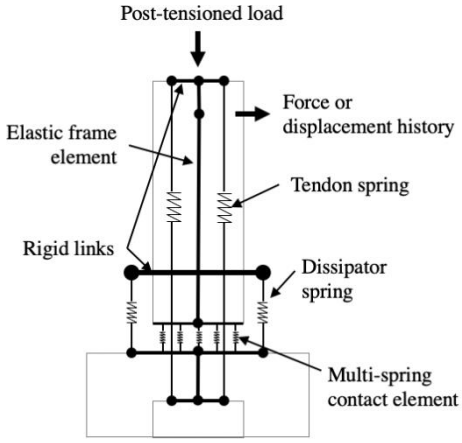

(c) Multi-spring model

Figure 1: Modelling techniques for cantilevered dissipative controlled rocking columns.

For simplicity, the models developed in this paper utilise bi-linear idealised curves used to represent the soil springs' force-deformation relationship or p-y response. To account for soil resistance on both sides of the pile, the force-deformation relationship of the springs was assumed to be identical in both transverse loading directions. The result was a backbone curve that adequately represented the compression-only soil on both sides of the pile using a single spring element [10].

No allowance had been made for the effects of inelastic soil deformation, lateral spreading, down-drag forces, or liquefaction on the pile foundation. The numerical models described in this paper are first used to define the loading protocol applied at the pile head in the experiment. Following the experimental phase, the two modelling solutions are compared to the experimental results described in Piras et al. [8] to confirm the effectiveness and accuracy of the modelling techniques.

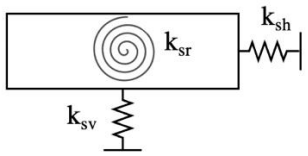

(a) Uncoupled spring model

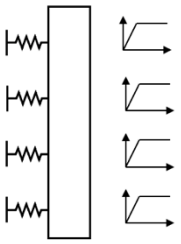

(b) p-y lateral springs

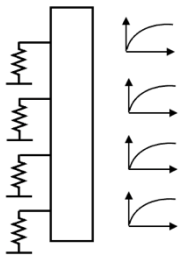

(c) t-z axial deformation springs

Figure 2: Idealised analytical modelling solutions for pile foundations with SSI.

EXPERIMENTAL VALIDATION

A cantilever DCR bridge column scaled at one-third has been experimentally tested at the University of Canterbury, as shown in Figure 3. The column is post-tensioned for self-centring and has fully threaded dissipating bars at the rocking joint [8]. The pier consists of a 500mm diameter column with a design height of 2.1m and is supported on a 600mm diameter monopile foundation.

The post-tensioning bar is 50mm in diameter and debonded the entire column length. The dissipative devices used in the specimen are eight Grade 300 fully threaded M17 steel rods. The dissipaters are connected to the permanent column and pile longitudinal reinforcement through threaded couplers. An internal shear key is provided at the rocking joint, which offers shear and torsion restraint and protection at the rocking surface. The stress-strain behaviour of the concrete is assumed to be linear elastic. This assumption can be made since a steel shear key will be used at the rocking surface, which will prevent interface damage.

Table 1 summarises the material characteristic properties adopted.

Experimental Setup

The experimental programme has been conducted to obtain experimental evidence to validate the numerical models. The test setup consists of two hydraulic actuator that load the pier transversely at the column and pile, as shown in Figure 4. The position of the ram and magnitude of loading at the column is chosen to simulate transverse inertial loading of the specimen from the superstructure. Only uni-axial transverse loading is considered because longitudinal displacements are typically not considered in bridges with a straight alignment due to the lock-in effect at the abutments. The position of the ram and magnitude of loading at the pile is designed to mimic the passive soil resistance in the pile. A third ram is also attached at the mid-height of the column to prevent out-of-plane movement; however, this ram is not loaded.

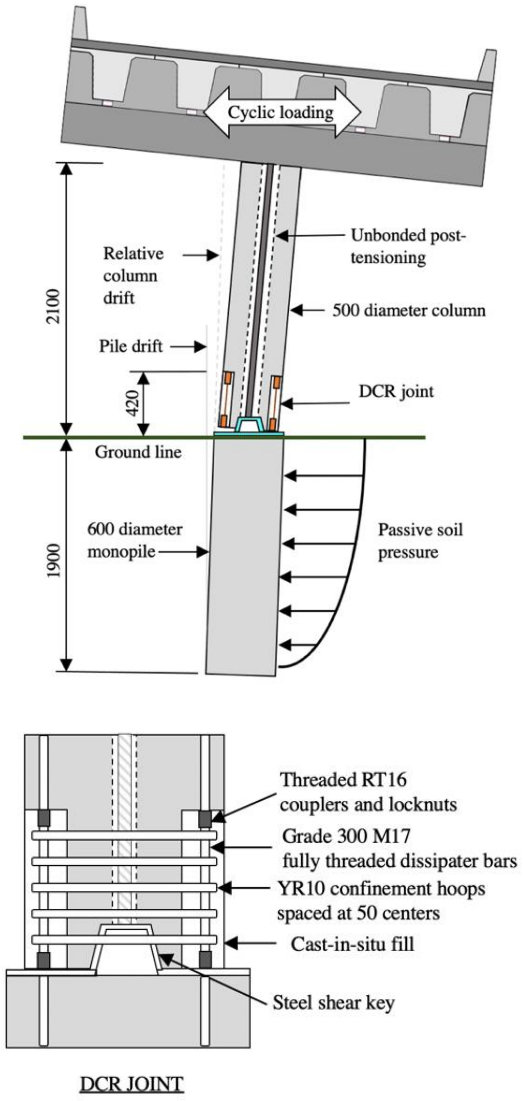

Figure 3: Cantilevered bridge pier with a DCR connection at the column-pile connection. Units are in millimetres.

Table 1: Material properties for the DCR column and monopile.

Reinforced concrete	
28-day compressive strength	40MPa
Modulus of elasticity	30GPa
In-situ grout at joint	
Measured 7-day compressive strength	50MPa
Mild steel reinforcement (Grade 500E)	
Yield Strength	500MPa
Steel Modulus	200GPa
Mild Steel Dissipaters (Grade 300)	
Tensile area	168.7mm^2
Steel modulus	148GPa
Yield strength	380MPa
Ultimate strength	560MPa
Post-tensioning (Grade 1030) [11]	
Steel modulus	170GPa
0.1% proof stress	835MPa
Ultimate tensile stress	1030MPa

Preliminary numerical models were used to define the loading protocol at the pile head and approximate the point of zero moment in the pile. The behaviour of the pile in the experiment is simplified as a rigid cantilever supported on a pin. In actuality, the pile will experience curvature along its length. In this research, the response along pile length is not of interest. Instead, the displacement and rotation at the pile head are essential to understanding how the pile influences the response of the post-tensioned rocking column. A more accurate representation of the pile response could be achieved with a longer pile tested with more hydraulic actuator or in a soil box. The experimental set-up adopted in this research took a simplified and economical approach that did not result in discrepancies with the numerical model observations. The numerical models, later described, also utilised a pin support at the bottom of the pile to replicate the experimental results.

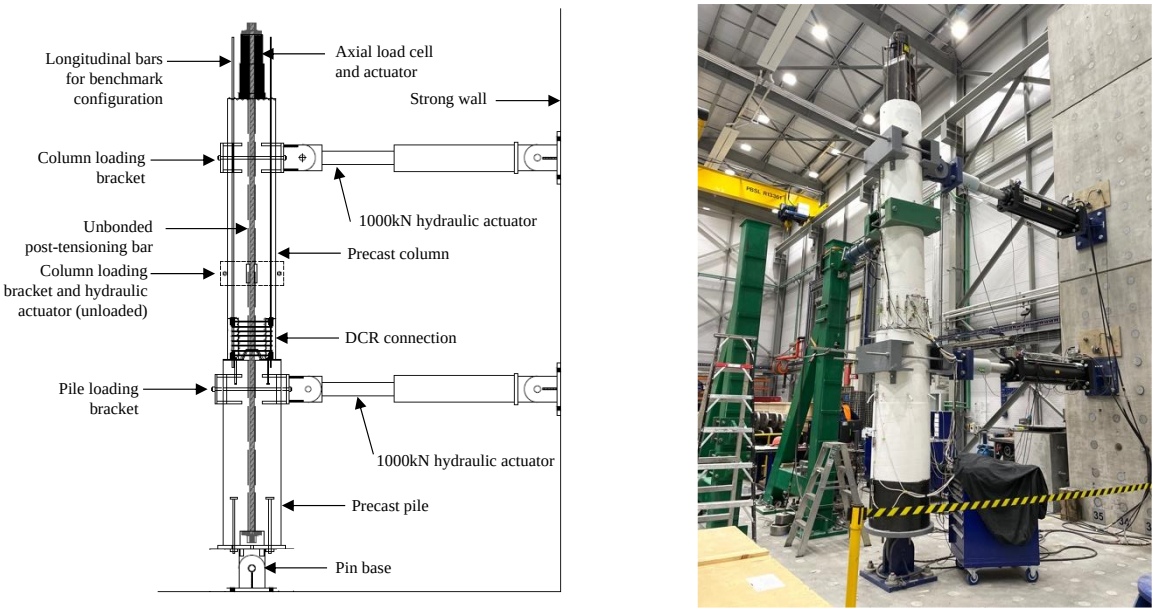

Figure 4: Schematic illustration and photographic image of the test setup for 1/3-scaled bridge pier with DCR connection.

Table 2: Soil properties.

Soil	Unit weight (kg/m^3)	Young's modulus (E') (kPa)	Effective friction angle (ϕ') (deg)
Loose sand	1442	20,000	30
Medium-dense sand	1560	48,000	40
Dense sand	1746	81,000	45

The variable control between tests was passive soil resistance, or loading protocol, from the hydraulic actuator at the pile. Three soil conditions – loose, medium-dense and dense sand – represent the variability in soil stiffness. The soil properties reported in Table 2 are used to define the soil spring stiffness, which is derived from the recommendations in NAVFAC [12], USACE [13] and Meyerhof [14]. The bridge in this research could have been founded on any soil type; however, characteristics of typical sandy soils in Christchurch were selected to define the soil springs [15].

NUMERICAL SOLUTIONS

This section briefly summarises the procedures adopted to carry out an analytical solution using the revised Monolithic Beam Analogy (rMBA) method, rotational spring model and multi-spring model. A method for modelling the monopile foundation and soil springs is also presented as the effects of SSI can influence the behaviour of a DCR column.

Revised Monolithic Beam Analogy Method

The rMBA method is used to define the multi-linear response of a DCR column. Additionally, it is used to define and calibrate the rotational spring and multi-spring model parameters later described. The rMBA method involves defining the response of the DCR column at three steps:

1. response up to decompression,
2. response up to yield, and
3. post-yield response.

The total moment capacity of the DCR connection is given by the combination of the post-tensioning (M_{PT}), axial load (M_N) and energy dissipaters (M_s).

$$M_{TOT} = M_{PT} + M_N + M_s \quad (1)$$

The re-centring ratio λ, which dictates the system's overall energy dissipation and self-centring behaviour, is a function of the post-tensioning, dissipaters and axial load. To allow for adequate self-centring and energy dissipation, a λ ratio between 1.15 to 1.5 is recommended [16,17].

$$\lambda = \frac{M_{PT}+M_N}{2M_S} \quad (2)$$

As the column displaces from its resting position, a gap opening forms at the rocking joint, like that shown in Figure 5. The gap opening causes extension of the post-tensioning bar or strands (Δ_{PT}) which incrementally increases the post-tensioning force (ΔT_{PT}), as depicted in Figure 6. The extension in the post-tensioning bar or strand is spread over the full unbonded length ($l_{ub,PT}$) of the bar or strand to ensure that it remains elastic at the design level drift.

The resulting post-tensioning force is the summation of the incremental and initial ($T_{PT,i}$) post-tensioning forces Where n is the number of gap openings, which is one for columns with single curvature and two for columns in double curvature; θ is the base rotation; c is the neutral axis depth; and E_{PT} and A_{PT} is the Young's modulus and area of the post-tensioning bar/stand.

$$\Delta_{PT} = n\theta\left(\frac{D}{2} - c\right) \quad (3)$$

$$\Delta T_{PT} = \frac{\Delta_{PT}}{l_{ub,PT}} E_{PT} A_{PT} \quad (4)$$

$$T_{PT} = \Delta T_{PT} + T_{PT,i} \quad (5)$$

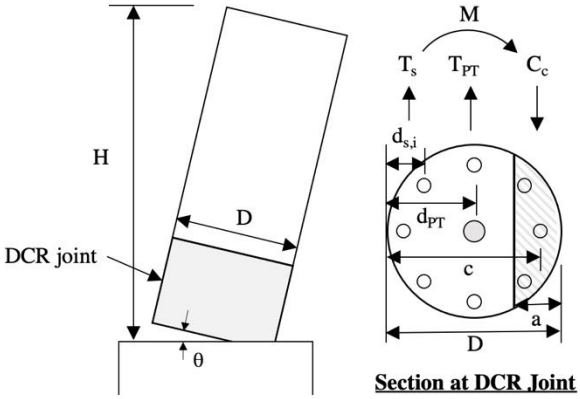

Figure 5: DCR column response at rocking.

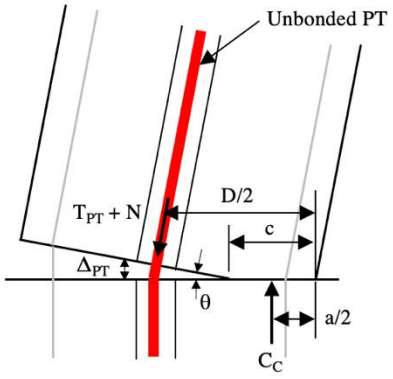

Figure 6: Internal forces in unbonded post-tensioning bar from rocking.

Similarly, as the column displaces, the steel dissipaters extend ($\Delta_s(i)$) inducing stresses on the bars (Figure 7). Because the steel dissipaters are unbonded, the bar strain is uniformly distributed over their lengths ($l_{ub,s}$).

$$\Delta_s(i) = \theta(d(i) - c) \quad (6)$$

$$\varepsilon_s(i) = \frac{\Delta_s(i)}{l_{ub,s}} \quad (7)$$

In Equation 6, *d(i)* is the depth of the steel layer being considered.

The bi-linear stress-strain response of the steel dissipaters is defined by Equation 8 and 9, where ε_y is the yield strain of the dissipating bars, r is the bi-linear factor commonly taken as 0.8% for mild steel dissipaters, and E_s is the Young's modulus of the steel dissipaters.

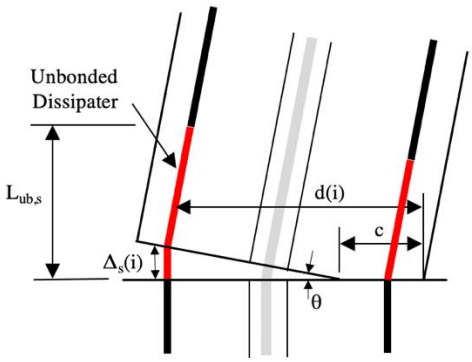

Figure 7: Internal forces in unbonded dissipating bars from rocking.

$$f_s(i) = \varepsilon_s(i)E_s \quad \text{for } \varepsilon_s(i) < \varepsilon_y \tag{8}$$

$$f_s(i) = f_s\left(1 + r\left(\frac{\varepsilon_s(i)}{\varepsilon_y} - 1\right)\right) \quad \text{for } \varepsilon_s(i) > \varepsilon_y \tag{9}$$

The resulting force in each steel layer is computed using Equation 10, where A_s is the bar area in each layer.

$$T_s(i) = f_s(i)A_s(i) \tag{10}$$

The moment contribution from the post-tensioning, axial load (N) and dissipaters is computed using Equations 11 to 13. Where D is the diameter of the column, and β is a concrete stress block factor that can be obtained from the design tables in the PRESSS Design Handbook [17].

$$M_{PT} = T_{PT}\left(\frac{D}{2} - \frac{\beta c}{2}\right) \tag{11}$$

$$M_N = N\left(\frac{D}{2} - \frac{\beta c}{2}\right) \tag{12}$$

$$M_s = \sum T_s(i)\left(d(i) - \frac{\beta c}{2}\right) \tag{13}$$

Response up to Decompression

The moment (M_{dec}) and displacement (Δ_{dec}) required to initiate a gap opening are referred to as the decompression force and displacement. Up until the point of decompression, only the axial force (N) and initial post-tensioning force ($T_{PT,i}$) act on the system.

$$M_{dec} = \frac{T_{PT,i}+N}{A} \cdot Z \tag{14}$$

$$\Delta_{dec} = \frac{2}{3}\theta_{col}H_c + \theta_{col}(H - H_c) \tag{15}$$

In Equations 14 and 15, Z is the section modulus of the column, θ_{col} is the column rotation, which is a function of the curvature ϕ_{col}, H and H_c are the column's cantilever height and clear height, respectively.

$$\phi_{col} = \frac{M_{dec}}{EI} \tag{16}$$

$$\theta_{col} = \frac{\phi_{col}H_c}{2} \tag{17}$$

At the decompression point, the base rotation is zero.

Response up to Yield

After the column has surpassed its decompression point, the base rotation is initiated, which engages the force response from the post-tensioning and steel dissipaters.

The base curvature, column rotation, elastic deflection and base rotation at yield are computed using Equations 18 to 21.

$$\phi_{col} = \frac{M_y}{EI} \tag{18}$$

$$\theta_{col} = \frac{\phi_{col}H_c}{2} \tag{19}$$

$$\Delta_{e,y} = \frac{\phi_{col}H_c^2}{3} + \theta_{col}(H - H_c) \tag{20}$$

$$\theta_y = \frac{\Delta_y - \Delta_{e,y}}{H} \tag{21}$$

The yield displacement (Δ_y) is iterated on until the maximum strain ($\epsilon_{s,max}$) is equal to the yield strain (ϵ_y) of the dissipaters.

$$\Delta_y(i+1) = \frac{\varepsilon_y}{\epsilon_{s,max}}\left(\Delta_y(i) - \Delta_e(i)\right) + \Delta_e(i) \tag{22}$$

The yield moment is the summation of the moment contributions from the axial load, post-tensioning and steel dissipaters.

$$M_y = M_{PT} + M_N + M_s \tag{23}$$

Post-Yield Response

The procedure for determining the post-yield response of the DCR column is similar to the approach adopted for the response at yield. The ultimate displacement demand (Δ_u) at MCE is defined as 1.5 times the design displacement demand (Δ_d) at ULS as specified in the New Zealand Bridge Manual [19].

$$\phi_{col} = \frac{M_u}{EI} \tag{24}$$

$$\theta_{col} = \frac{\phi_{col}H_c}{2} \tag{25}$$

$$\Delta_{e,u} = \frac{\phi_{col}H_c^2}{3} + \theta_{col}(H - H_c) \tag{26}$$

$$\theta_u = \frac{\Delta_u - \Delta_{e,u}}{H} \tag{27}$$

The ultimate moment is the sum of the moment contributions from the axial load, post-tensioning and steel dissipaters.

$$M_u = M_{PT} + M_N + M_s \tag{28}$$

The resulting backbone moment-ration response of the DCR column is graphed in Figure 8.

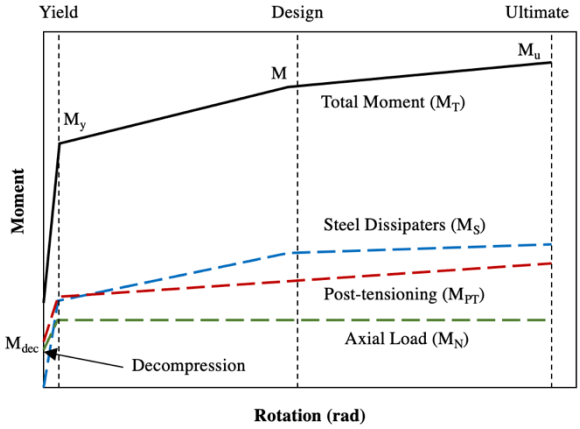

Figure 8: Moment-rotation response of DCR column.

Rotational Spring Model

Rotational spring models provide a simplified modelling solution that consists of coupled rotational springs. The contributions from re-centring and dissipation are modelled using a multi-linear elastic hysteresis for the re-centring rotation spring and an elastic-plastic relationship for the dissipative contributions. The two rotational springs are in parallel and have zero length, as shown in Figure 9.

The rMBA design method, previously described, is carried out to define the moment rotation response of the prestressing, which also includes axial load contribution. A nonlinear

inelastic hysteresis model is defined for the mild steel dissipaters. A kinematic hysteresis rule is adopted for internal dissipaters. Whereas a Ramberg-Osgood steel rule [20] describes the nonlinear hysteretic behaviour if external dissipaters are adopted.

The rotational spring model has the advantage of having low computational effort without compromising accuracy; however, the outputs are limited and do not capture the local behaviour of the DCR system (i.e. response of post-tensioning bar and dissipaters, and section neutral axis).

Appendix 1 contains a detailed worked example with the procedure for determining the moment-rotation response of the axial load and post-tensioning.

Multi-Spring Model

An advantage of using a multi-spring model is the simulation of the rocking interface, which is modelled by two parallel rigid beams and compression-only nonlinear gap links connecting the beams, as shown in Figure 10. The nonlinear gap springs are defined vertically and fixed in the lateral directions. The minimum length of gap links in SAP2000® is 10mm; however, the gap length should be left as the default value of zero when defining the link element.

To define the initial stiffness of the gap springs, Liu [21] found that the Gauss-Lobatto quadrature rule [22] is not readily applicable to circular rocking columns but is a reliable solution for rectangular columns. Instead, multi-dimensional numerical integration (cubature) rules provide a better method for defining the multi-spring element for circular rocking sections using the circular domain adopted from Abramowitz and Stegun [23].

The total stiffness of the rocking interface (k_{int}) is calculated using Equation 29 and distributed over the rocking surface.

$$k_{int} = \frac{E_c A_c}{I_{eff}} \tag{29}$$

In computing k_{int}, an effective column length (I_{eff}) needs to be assumed. For an exterior joint, I_{eff} can be taken as the column diameter (D_c). The interface material is linear elastic with a modulus of elasticity (E_c) corresponding to concrete. A_c is the cross-sectional area of the column [24].

Due to multi-spring elements at the base of the column frame, the total stiffness of the column (k_c) is reduced. A magnified cross-sectional area (A^*_c) is assigned to the column frame elements to compensate for the reduced system stiffness. k_c is represented through the relationship in Equation 30.

$$\frac{1}{k_c} = \frac{1}{k_{int}} + \frac{H}{E_c A^*_c} = \frac{H}{A_c E_c} \tag{30}$$

H is the section height, A_c is the gross column area, and A^*_c is the increased cross-section area of the column to compensate for the increased flexibility of the multi-spring element. Increasing the cross-section area only affects the axial stiffness of the column, not the flexural stiffness. Equation 30 is rearranged to solve for A^*_c in Equation 31.

$$A^*_c = A_c \left[\frac{1}{1-(A_c \cdot E_c)/(H \cdot k_{int})}\right] \tag{31}$$

To model cracking behaviour due to flexural bending, cracked section properties are applied to the column's elastic frame elements. The column's modified stiffness is typically in the range of 0.3 to $0.4E_cI_g$, where I_g is the gross moment of inertia of the column section, depending on the axial load. Reference can also be made to NZS 3101 [16] for defining the cracked section properties of a concrete column.

Mild steel dissipaters are modelled as nonlinear plastic links. The dissipaters are connected transversely through two rigid beams that connect back to the column, as shown in Figure 10. The stiffness of each nonlinear spring is defined by Equation 32, where A_{ms} is the area of the mild steel dissipater bar and h_{dis} is the height of the dissipating bar.

$$k_{dis,i} = \frac{A_{ms,i} E_s}{h_{dis}} \tag{32}$$

The self-centring post-tensioned (PT) bar is assumed to remain elastic throughout the analysis and can be modelled as a tendon frame with an applied tension load in SAP2000® with linear elastic material stiffness. The tension load applied to the tendon should be from the designated jacking end. Most likely, this is at the top of the column.

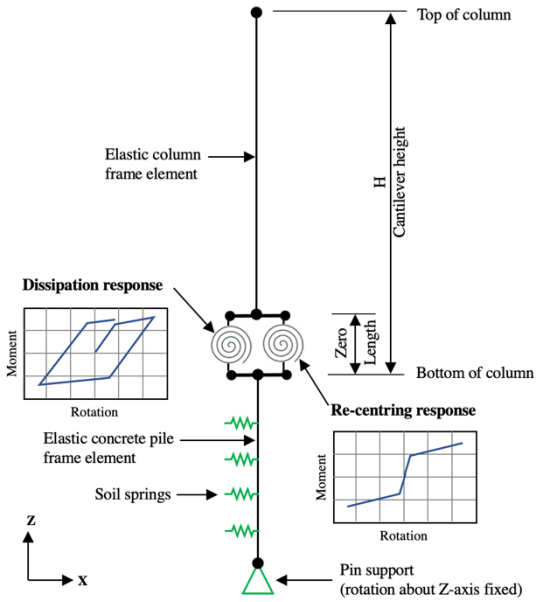

Figure 9: Rotational spring model with two rotational springs in parallel adopted for the cantilever bridge pier with DCR joint at the column-pile connection.

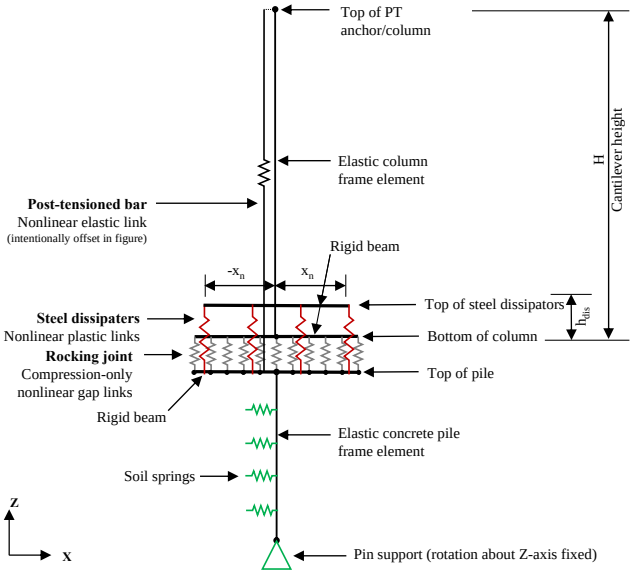

Figure 10: Two-dimensional multi-spring model adopted for the cantilever bridge pier with DCR joint at the column-pile connection.

To compensate for post-tensioning loss due to elastic shortening at load transfer, the initial post-tensioning force should be magnified using Equation 33 to ensure that the target post-tensioning force is achieved within the frame element.

$$T^*_{PT,i} = T_{PT,es} + T_{PT,N} \quad (33)$$

$$T_{PT,es} = T_{PT,i}\left[1 - \frac{A_{PT}E_{PT}}{A^*_c E_c}\right]^{-1} \quad (34)$$

$$T_{PT,N} = N\left[\frac{A_{PT}E_{PT}}{A^*_c E_c}\right] \quad (35)$$

$T_{PT,es}$ is the post-tensioning force after elastic shortening and $T_{PT,N}$ is the post-tensioning force after axial load application. A_{PT} and E_{PT} is the area and Young's modulus of the post-tensioning bar, respectively; A^*_c and E_c is the increased cross-sectional area and Young's modulus of the concrete column, respectively; N is the applied axial load.

The strain in concrete from elastic shortening is equal to the initial post-tensioning strain minus the strain due to elastic shortening (Equation 36). The strain relationship presented in Equation 34 can be used to relate force, area and Young's modulus in Equation 34 to compute the post-tensioning force after elastic shortening.

$$\epsilon_{c,es} = \epsilon_{pi} - \epsilon_{po,es} \quad (36)$$

Furthermore, the strain in the concrete is equal to the strain in the PT bar due to the axial load reaction (Equation 37) and can be used to relate force, area and Young's modulus in Equation 35 to compute the post-tensioning force after axial load application.

$$\epsilon_{c,N} = \epsilon_{PT,N} \quad (37)$$

Application of post-tensioning force induces strains in the steel dissipaters. These strains need to be considered when internal dissipaters are used since the column is post-tensioned after the dissipaters are installed, and the in-situ concrete is cured. However, when external dissipaters are used in a DCR system, the dissipaters are installed after the column is post-tensioned so that only the precast element is axially loaded. To ensure that the load in each dissipater is zero after the application of the initial post-tensioning force, Marriott [7] proposes a procedure in which a prestressing force is applied internally to each dissipater which puts the dissipaters into tension.

More detailed macro-models utilising multi-springs located along the rocking interface of a post-tensioned connection have been investigated by [24-26].

Calibrating the Multi-spring Model

To accurately determine the total stiffness of the multi-spring unit (k_{int}), a moment-rotation section analysis of the rocking joint is carried out using the rMBA method, which is described in detail in Palermo et al. [5]. It is recommended that the model be initially calibrated, assuming fixity at the base of the column (no rotations or displacements at the pile head) and checked against the results of the moment-rotation section analysis.

Calibration of the multi-spring model is carried out by computing the neutral axis depth of the macro-model using Equation 38, which utilises the first and last contact and takes into account that the first and last contact springs do not coincide with the true edges of the rocking section.

$$c = \frac{\mathrm{D}}{2}\left[\alpha\frac{\Delta_n+\Delta_1}{\Delta_n-\Delta_1} + 1\right] \quad (38)$$

where $\alpha = |2x_1/D| = |2x_n/D|$; $x_1 = -x_n$ and are the x-axis coordinates of the outermost contact springs; and Δ_1 and Δ_n are the signed vertical displacements in the outermost contact springs (refer to Figure 11); D is the column diameter. Refer to the design example in Appendix 1 to compute the neutral axis depth for a given column rotation or deflection.

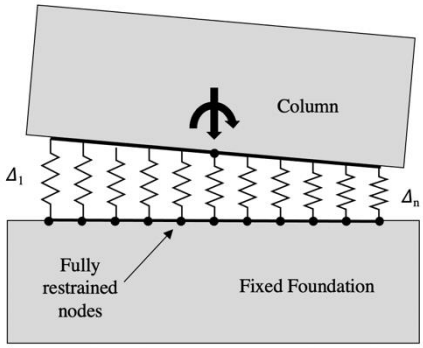

Figure 11: Contact springs for multi-spring model.

The section analysis and the macro-model are subjected to the same rotation demand during calibration. Calibration concerns three key section parameters: the moment capacity, the neutral axis position, and the centroid of the contact compression force. The centroid of the compression region can be computed by considering moment equilibrium of the section in Equation 39 in which $a/2$ is the depth to the centroid (from the compression edge of the section), d_{PT} is the distance from the compression edge of the section to the PT tendon, T_{PT} is the total force in the PT tendon and M is the base moment.

$$\frac{a}{2} = \frac{T_{PT}d_{PT} - M}{T_{PT}} \quad (39)$$

The axial stiffness of the multi-spring (k_{int}) is updated until convergence is achieved between the section analysis and the multi-spring macro model.

Foundation and Soil Springs

Especially in New Zealand, it is common for bridge columns to be supported by monopile foundations which can significantly influence the performance of a DCR column due to damping effects from the soil [27].

In a laterally loaded bridge, the load is resisted by the soil-structure interaction effect, which depends on the soil properties, pile material, pile diameter and loading type. The behaviour of a laterally loaded bridge pile can be understood from soil reaction-pile deflection (p-y) curves of the soil [28].

Today, the most well-known and used foundation model for soil-structure interaction by structural engineers is the Winkler model, in which the elastic foundation is modelled with springs that represent the subgrade [29].

In this research, the pile is modelled with elastic frame elements and elastic soil springs spaced vertically at a distance equal to the pile diameter (D_p). The base of the pile is supported by a pin to allow for rotations. Alternatively, the bottom of the pile can be modelled with a roller and or vertical spring to simulate translational and vertical displacements. Because this study is concerned with the relative displacement of the pier and differential rotations between the pile and column, the base of the pile is pinned to represent the expected point of contra flexure in a real soil-pile scenario. To simplify the single-degree-of-freedom two-dimensional analysis, the rotation about the global vertical axis is fixed to prevent torsional instability in the modal analysis.

Lateral soil springs can be developed using the Winkler Spring method, in which the soil pressure p is related to lateral deflection y through the coefficient of subgrade reaction k of a particular soil layer [30]. An elastic-perfectly plastic (bi-linear)

relationship is adopted for the soil springs, as shown in Figure 12.

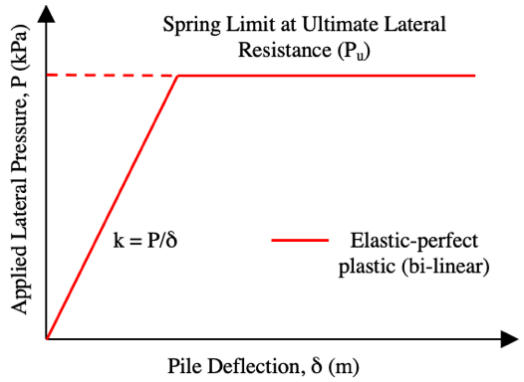

Figure 12: Bi-linear soil spring relationship.

The lateral spring stiffness or modulus of subgrade reaction (k_h, in units *kN/m/m*) is defined by Equation 40, where k is the coefficient of subgrade reaction (in units $kN/m^2/m$), and D_p is the pile diameter (in units *m*).

$$k = k\ D_p \tag{40}$$

Carter [31] and Ling [32] found that the formula in Equation 41 for the coefficient of subgrade reaction ($k = p/y$) produces the closest agreement in predicting the pile lateral deflection (y).

$$k_h = \left(\frac{E\prime}{1-\mu^2}\right) \sqrt[12]{\left(\frac{E\prime D_p^4}{E_p I_p}\right)} \tag{41}$$

where E' is the soil Young's modulus (in units kN/m^2), E_p is the pile material modulus of elasticity (in units kN/m^2), I_p is the pile second moment of inertia ($\frac{\pi D_p^2}{64}$ in units m^4), and μ is the Poisson's ratio of the soil.

For non-cohesive soils, the ultimate lateral resistance (P_u) per metre pile length is calculated using the effective soil overburden pressure (σ_v'), mobilised coefficient of passive earth pressure (k_p), pile diameter (D_p) and effective friction angle (ϕ') as defined by Equations 42 and 43.

$$P_u = 1.5 \times k_p \times \sigma_v' \times D_p \tag{42}$$

$$k_p = \frac{1+\sin(\phi\prime)}{1-\sin(\phi\prime)} \tag{43}$$

The p-y soil springs adopted are summarised in Table 3. Since the springs are assumed to remain elastic, P_u is not defined.

Table 3: P-y soil springs adopted in numerical models.

Soil	Lateral spring stiffness, k (kN/m)
Loose sand	4473
Medium-dense sand	11547
Dense sand	20355

NUMERICAL RESULTS AND DISCUSSION

The cyclic response of the test specimen in Figure 4 was validated using a rotational spring and multi-spring model in SAP2000®. The two numerical models described the specimen's behaviour in terms of its base moment-drift hysteretic response, as shown in Figure 13. The degradation of the experiment's hysteretic response, which results from concrete crushing at the rocking interface, is not represented in either the multi-spring or rotational spring model since they utilise elastic frame elements for the column. For this reason, it is recommended that a multi-spring and rotational spring model is used to represent the column's cyclic response up to a ULS-level seismic event when concrete crushing is expected to be initiated.

The multi-spring model unloads between steps when pushed, as demonstrated in Figure 13. This unloading phenomenon is caused by the model decreasing the load on the structure to reach convergence. Further developments on the model are required to address convergence issues.

The monotonic response or backbone curve derived using the rMBA method is also included in Figure 13. The elastic stiffness obtained from the rMBA method is higher as this numerical approach assumes a fixed base at the column's foundation. The influence of foundation flexibility delays the onset of column yielding, as proven in the experimental results and numerical models.

The multi-spring and rotational spring models' cyclic response was similar; however, the rotational spring model under-represented the DCR's hysteretic response as it approached the origin. The rotational spring model provides less computational effort to develop than the multi-spring model. However, the outputs from the rotational spring model are limited. The multi-spring model can describe the cyclic response of the post-tensioning bar, the section's neutral axis depth, and the steel dissipaters' cyclic response, as shown in Figures 14 to 16. While the axial stress in the dissipaters and neutral axis depth was well represented in the multi-spring model, the post-tensioning force was overestimated compared to the experimental results.

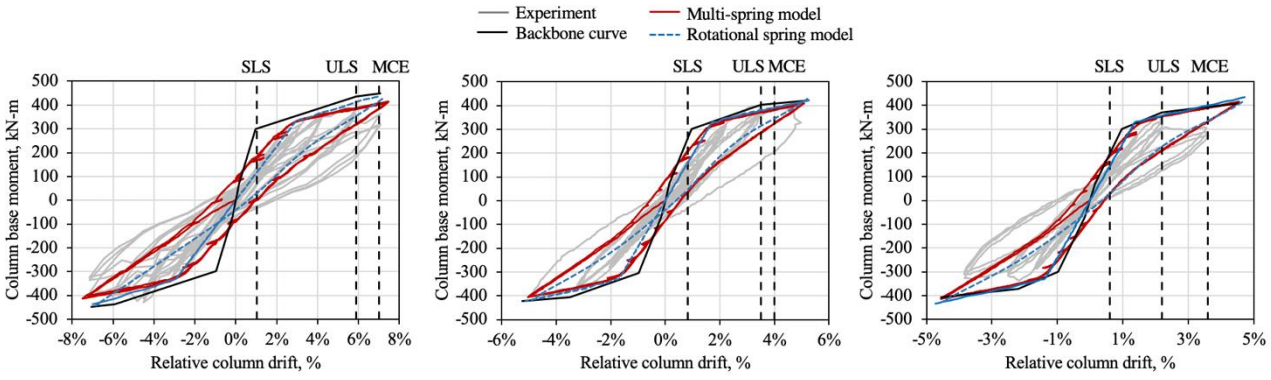

(a) Loose sand ***(b) Medium-dense sand*** ***(c) Dense sand***

Figure 13: Comparison of experimentally-derived and numerically simulated moment-drift response.

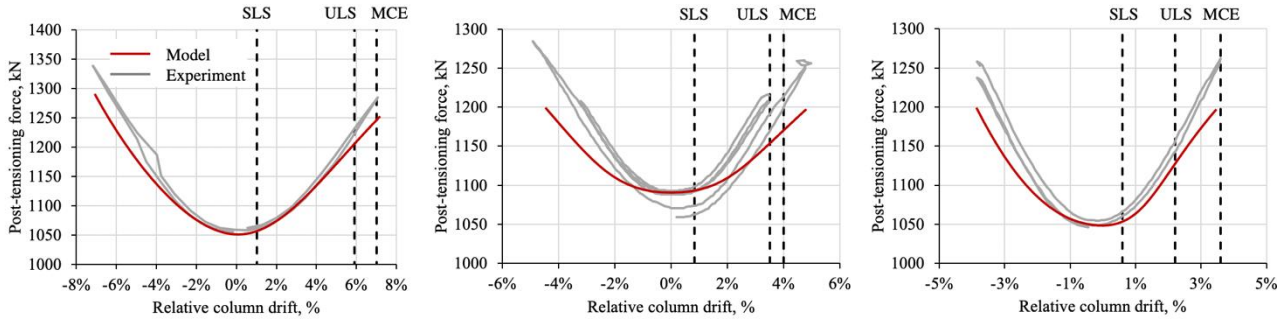

(a) Loose sand *(b) Medium-dense sand* *(c) Dense sand*

Figure 14: Comparison of post-tensioning force in multi-spring model with experimental data.

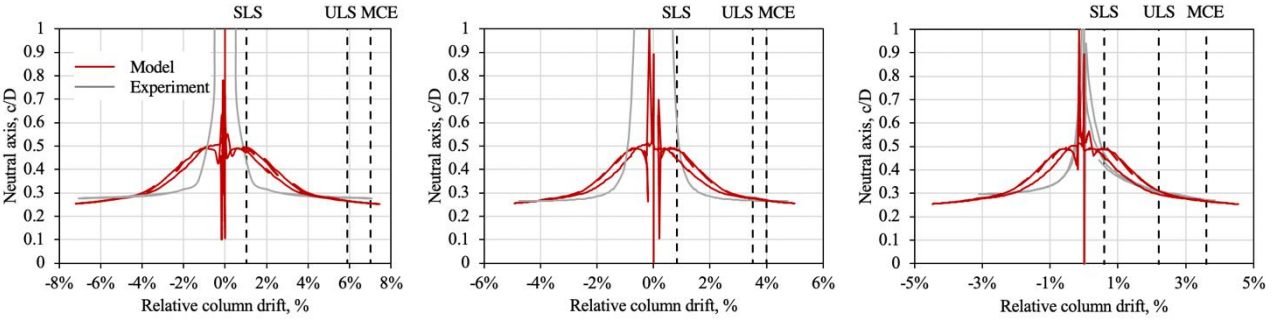

(a) Loose sand *(b) Medium-dense sand* *(c) Dense sand*

Figure 15: Comparison of neutral axis depth in multi-spring model with experimental data. Some experimental data has been omitted for clarity.

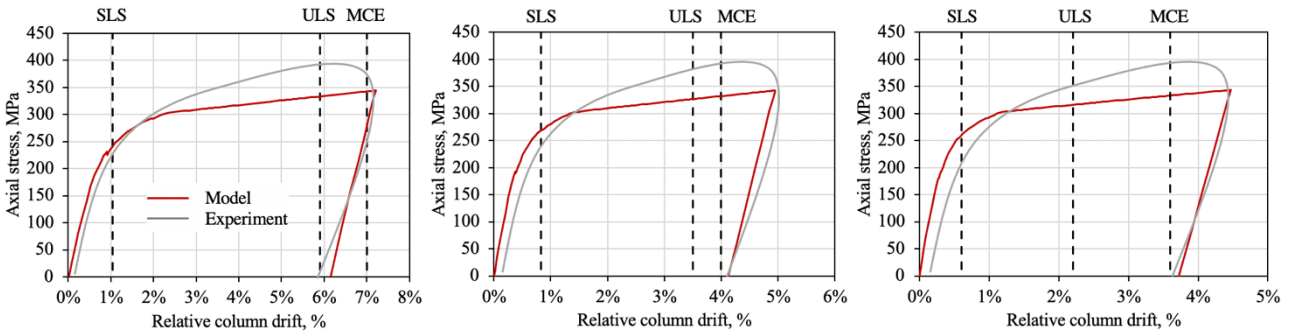

(a) Loose sand *(b) Medium-dense sand* *(c) Dense sand*

Figure 16: Comparison of axial stress in steel dissipater in multi-spring mode with experimental data. Some experimental data has been omitted for clarity.

As drift increases, the concrete cover crushes and reduces the post-tensioning force, as demonstrated in the experimental results. However, the concrete column used in the multi-spring model is represented by an elastic frame element with no strength degradation capabilities. Because the concrete is not losing strength with increased cyclic loading, the post-tensioning force is greater in the numerical model than in the experimental results. Thus, the overall column stiffness increases rather than decreases, as shown in the moment-drift hysteresis response in Figure 13. The post-tensioning force in Figure 14 further demonstrates that as concrete crushing is initiated at approximately 2% relative column drift, the post-tensioning force in the multi-spring model continues to increase because there is no reduction in concrete stiffness. As the drift increases, the experimental and numerical response variability increases.

Potentiometers were used to measure the uplift at the rocking joint, as shown in Figure 17, which was used to estimate the neutral axis depth of the section using strain compatibility analysis. The neutral axis depth, normalised by the section depth, estimated from the experiment and multi-spring model, is plotted in Figure 15. The neutral axis response of the column was similar for the experiment and numerical model. The neutral axis approaches zero or infinity as the column rocks about its centre. As drift increases, the neutral axis depth plateaus to 20-30% of the section depth.

In the experiment, the gap openings at the rocking joint were also used to estimate the axial stress in the internal dissipaters. The stress in the dissipaters resembled the predicted response in the multi-spring model, as shown in Figure 16. Discrepancies in the axial stress at larger drifts could be attributed to the dissipaters slightly buckling during the experiment when in compression, which allowed for larger gap openings.

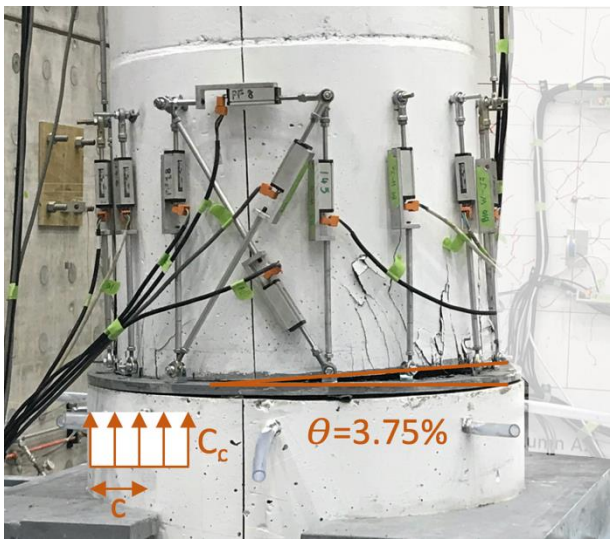

Figure 17: Crushed concrete cover as a result of column rocking.

Modelling Limitations in SAP2000®

SAP2000® is a structural analysis and design software commonly used by practising structural engineers due to its user-friendly graphical user interface and computational capabilities. However, like any computational software, SAP2000® has limitations when modelling post-tensioned rocking columns. The authors identify the following limitations:

- The rocking interface can be modelled using a series of compression-only springs. However, SAP2000® is limited to a minimum spring length of 10mm, rather than zero-length springs. This will reduce the stiffness of the column. For this reason, the cross-sectional area of the column is magnified to compensate for the reduced stiffness (refer to Equation 31).
- The concrete is modelled as an elastic frame element with no strength degradation. As a result, loss in column stiffness due to concrete crushing is not represented. This research has found that this can result in a margin of error up to 5%.
- The post-tensioning force is under estimated for large drifts in the SAP2000® model, which can result in under designing the DCR connection. The proposed analytical solution has shown to be an effective tool to design the column at the design drift limit state but can result in some error at the collapse limit state.

CONCLUSIONS

This paper provides a numerical tool to evaluate the monotonic and cyclic behaviour of a dissipative controlled rocking (DCR) bridge pier supported on a monopile foundation embedded in sand. A rotational spring model and a multi-spring model have been implemented using SAP2000® software. The pile-soil system is modelled with an elastic frame element connected to vertically-spaced soil springs. Moreover, to account for soil-structure interaction (SSI) effects, loose sand, medium-dense sand and dense sand conditions are considered. The results from an experimental programme carried out by the authors at the University of Canterbury are then used to validate the numerical solutions.

The following main conclusions can be derived from this numerical study:

- Simulation results from both the rotational spring model and the multiple-spring model are found to be in good agreement with the experimental ones for all the three sand conditions examined;
- From a computational viewpoint, the relatively simple mathematical formulation and easy implementation makes the rotational spring model preferable over the multi-spring model, especially if complex Multi-Degree-of-Freedom structures are considered; yet, its predictive capability is limited to the monotonic response of bridge piers with DCR connections;
- In contrast, the multi-spring model is a more resourceful tool from an output viewpoint. Such a model can also describe the cyclic response of the DCR pier, including the moment-drift hysteresis, cyclic response of the post-tensioning and steel dissipaters, and gap-opening interface rocking characteristics.
- The Winker model provided a reliable method to develop force-displacement (p-y) relationships to represent the SSI.
- The research outcomes are aligned with past research carried out by Mashal [33] and Marriott [7], where different DCR solutions, or rocking connection details, were explored.

ACKNOWLEDGMENTS

The authors would like to express their gratitude to QuakeCoRE, Ancon, Freyssinet, Sika, Contech, Everitt Site Supplies, and iNFORCE for their financial support and material donations. Additionally, the authors would like to acknowledge Compusoft Engineering Ltd. for providing technical support and SAP2000® modelling recommendations.

REFERENCES

1 Stone WC, Cheok GS and Stanton JF (1995). "Performance of hybrid moment-resisting precast beam column concrete connections subjected to cyclic loading". *ACI Structural Journal*, **92**(2): 229–249.

2 Priestley M (1996). *"Seismic Design and Retrofit of Bridges"*. John Wiley and Sons, Inc.

3 Federation Internationale du Béton (FIB) (2007). "*Seismic Bridge Design and Retrofit - Structural Solutions*". FIB Bulletin No. 39.

4 Pampanin S, Priestley MJ and Sritharan S (2001). "Analytical modelling of the seismic behaviour of precast concrete frames designed with ductile connections". *Journal of Earthquake Engineering*, **5**(3): 329-367. https://doi.org/10.1080/13632460109350397

5 Palermo A, Pampanin S and Calvi G (2004). "Use of 'controlled rocking' in the seismic design of bridges". *13th World Conference on Earthquake Engineering*, 2006 August 1-4, Vancouver, B.C., Canada.

6 Federation Internationale du Béton (FIB) (2003). *"Seismic Design of Precast Concrete Building Structures"*. B Bulletin 39, International Federation for Structural Concrete, Lausanne, Switzerland.

7 Marriott D (2009). *"The Development of High-Performance Post-Tensioned Rocking Systems for the Seismic Design of Structures"*. PhD Dissertation, University of Canterbury, Christchurch, NZ.

8 Piras S, Palermo A and Chiaro G (2022). "Quasi-static cyclic testing of hybrid post-tensioned bridge column supported on a monopile foundation". *Journal of Bridge Engineering*, **27**(11). https://doi.org/10.1061/(ASCE)BE.1943-5592.0001962

9 Oliver S, Hare J and Harwood N (2013). "Soil structure interaction starts with engineers". *Proceedings of the 2013 NZSEE Conference*, 26-28 April, Wellington, NZ.

10 Wotherspoon L (2009). *"Integrated Modelling of Structure-Foundation Systems"*. PhD Dissertation, University of Auckland, Auckland, NZ.

11 Freyssinet (2017). *Freyssinet Prestressing*. https://www.freyssinet.co.nz/sites/default/files/freyssinet_prestressing.pdf

12 NAVFAC (1986). "*Soil Mechanics Design Manual* 7.01". Naval Facilities Engineering Command, Washington, DC, USA.

13 USACE (1990). *"Settlement Analysis"*. US Army Corps of Engineers, Washington, DC, USA.

14 Meyerhof G (1956). "Penetration tests and bearing capacity of cohesionless soils." *Journal of the Soil Mechanics and Foundations Division*, **82**(1). https://doi.org/10.1061/JSFEAQ.0000001

15 Stringer ME, Taylor ML and Cubrinovski M (2015). *"Advanced Soil Sampling of Silty Sands in Christchurch"*. Internal Report, University of Canterbury, Christchurch, NZ.

16 Standards New Zealand (2006). "*NZS 3101 Concrete Structures Standard: Part 1 - The Design of Concrete Structures*". Standards New Zealand, Wellington, NZ.

17 Pampanin S, Marriott D, Palermo A and Bolognini D (2010). *"PRESSS Design Handbook"*. New Zealand Concrete Society, Auckland, NZ.

18 Wacker JM, Hieber DG, Stanton JF and Eberhard MO (2005). "*Design of Precast Concrete Piers for Rapid Bridge Construction in Seismic Regions*". Report No. WA-RD 629.1, University of Washington, Seattle, USA.

19 NZTA (2018). "*Bridge Manual, Third Edition*". New Zealand Transport Agency, Wellington, NZ.

20 Ramberg W and Osgood WR (1943). *"Description of Stress-Strain Curves by Three Parameters"*. Technical Note 902, National Advisory Committee on Aeronautics.

21 Liu R (2018). *"Multi-Performance Seismic Design of Low Damage Bridge"*. PhD Dissertation, Department of Civil and Natural Resources Engineering, University of Canterbury, Christchurch, NZ.

22 Davis PJ and Rabinowitz P (2007). "*Methods of Numerical Integration*". Courier Corporation.

23 Abramowitz M and Stegun IA (1965). *"Chapter 25: Numerical Interpolation, Differentiation, and Integration"* in *Handbook of Mathematical Functions: with Formulas, Graphs, and Mathematical Tables*". Dover Publications: New York, USA.

24 Spieth HA, Carr AJ, Pampanin S, Murahidy AG and Mander JB (2004). "*Modelling of Precast Prestressed Concrete Frame Structures with Rocking Beam-Column Connections*." Research Report 2004-01, University of Canterbury, Christchurch, NZ.

25 Kim J (2002). "*Behavior of Hybrid Frames under Seismic Loading*". University of Washington, Seattle, USA.

26 Palermo A, Pampani, S and Carr AJ (2005). "Efficiency of simplified alternative modelling approaches to predict the seismic response of precast concrete hybrid systems." *fib Symposium*, Budapest, Hungary.

27 Palermo A, Liu R, Rais A, McHaffie B, Andisheh K, Pampanin S, Gentile R, Nuzzo I, Granerio M, Loporcaro G, McGann C and Wotherspoon L (2017). "Performance of road bridges during the 14 November 2016 Kaikoura earthquake." *Bulletin of the New Zealand Society for Earthquake Engineering*, **50**(2): 253–270. https://doi.org/10.5459/bnzsee.50.2.253-270

28 Kavitha PE, Beena KS and Narayanan KP (2016). "A review on soil-structure interaction analysis of laterally loaded piles". *Innovative Infrastructure Solutions*, **1**(1): 1-15.

29 NEHRP (2012). *"Soil-Structure Interaction for Building Structures."* Report no. NIST GCR12-917-21.

30 Kerr A (1984). "On the formal development of elastic foundation models". *Ingenieur-Archive*. **54**(6): 455-464.

31 Carter DP (1984). *"A Nonlinear Soil Model for Predicting Lateral Pile Response"*. Master Thesis, University of Auckland, Auckland, NZ.

32 Ling LF (1988). *"Back Analysis of Lateral Load Tests on Piles"*. Master Thesis, Department of Civil and Environmental Engineering, University of Auckland, Auckland, NZ.

33 Mashal M (2015). *"Post-Tensioned Earthquake Damage Resistant Technologies for Accelerated Bridge Construction*". PhD Dissertation, Department of Civil and Natural Resources Engineering, University of Canterbury, Christchurch, NZ.

APPENDIX A. MONOTONIC RESPONSE WORKED EXAMPLE

Geometry

Column diameter	D = 500mm
Column area	A = 196349.5mm^2
Gross moment of inertia	$I = \frac{1}{4}\pi\left(\frac{D}{2}\right)^4 = 0.003m^4$
Effective moment of inertia	$I_e = 0.3I = 0.001m^4$
Column section modulus	$Z = \frac{I}{D/2} = 0.012m^3$
Clear column height	H = 2.1m
Cantilever height	H_c = 2.1m
Axial load reaction	N = 210kN

Material Properties

Concrete

Concrete compressive strength	f'$_{ce}$ = 52MPa
Concrete modulus of elasticity	E_{ce} = 33892MPa

Dissipaters

Yield strength	f_y = 380MPa
Bar diameter	$d_{b,e}$ = 16mm
Bar area	$A_{b,e}$ = 168.7mm^2
Number of bars	N_b = 8

Transverse hoops

Yield strength	f_{yh} = 500MPa
Bar diameter	d_{bh} = 10mm
Bar area	A_{bh} = 78.54 mm^2
Bar spacing	s = 50mm

Post-tensioning bar

Yield stress	$f_{PT,y}$ = 835MPa
Fracture stress	$f_{PT,u}$ = 1030MPa
Modulus of elasticity	E_{PT} = 205GPa
Bar diameter	D_{PT} = 50mm
Bar area	A_{PT} = 1963mm^2
Number of bars	N_{PT} = 1

Refer to Figure 3 for details of the DCR column used in this example.

Part 1: DCR Response at the Design Moment (ULS-Level Seismic Event)

Design displacement target (3.25% design column drift)

Δ_d = 68.3mm

Design moment

$$M = 156kNm$$

Design Gap Opening

Base curvature

$$\phi_{col} = \frac{M}{E_{ce}I_e} = 0.00501\ 1/m$$

Rotation at top of column

$$\theta_{col} = \frac{\phi_{col}H_c}{2} = 0.00526 \text{ rad}$$

Elastic displacement demand

$$\Delta_e = \frac{2}{3}\theta_{col}H_c + \theta_{col}(H - H_c) = 0.007\ m$$

Design gap opening

$$\theta = \frac{\Delta_d - \Delta_e}{H} = 0.029\ rad$$

Post-Tensioning Design

Target re-centring ratio

λ = 1.5

Re-centring contribution to moment capacity

$$\alpha_{OTM} = \frac{\lambda}{0.5+\lambda} = 0.75$$

Post-tensioning moment contribution

$$M_{PT} + M_N = \alpha_{OTM}M_T = 117kNm$$

$$M_{PT} + M_N = (T_{PT} + N)\left(\frac{D}{2} - \frac{a}{2}\right)$$

Centroid of the concrete compressive block

$$\frac{a}{2} = \frac{\beta c}{2} = 0.085m$$

Assumed neutral axis depth (20% D)

$$c = 0.2 \cdot 0.5m = 0.1m$$

Assumed stress block factor

$$\beta = 0.85$$

Total axial load required

$$T_{PT} + N = \frac{M_{PT} + M_N}{\left(\frac{D}{2} - \frac{a}{2}\right)} = 565kN$$

Post-tensioning force

$$T_{PT} = 565kN - N = 355kN$$

Number of gap openings

$$n = 1$$

Tendon extension at design gap opening

$$\Delta_{PT} = n\theta\left(\frac{D}{2} - c\right) = 0.0043m$$

Unbonded length of post-tensioning bar (height of column and pile)

$$l_{ub,PT} = 4.482m$$

Additional post-tensioning load due to gap opening

$$\Delta T_{PT} = \frac{\Delta_{PT}}{l_{ub,PT}} E_{PT} A_{PT} = 391kN$$

Minimum initial post-tensioning load

$$T_{PT,i} = T_{PT} - \Delta T_{PT} << 0\text{kN}$$

Use $T_{PT,i} = 900kN$

Total post-tensioning force

$$T_{PT} = T_{PT,i} + \Delta T_{PT} = 1291kN$$

Dissipating Bar Force

Unbonded bar length

$$l_{ub} = 360mm$$

Bi-linear factor

$$r = 0.008$$

Bar extension

$$\Delta_s(i) = \theta(d(i) - c)$$

Bar strain

$$\varepsilon_s(i) = \frac{\Delta_s(i)}{l_{ub,s}}$$

Bar stress

$$f_s(i) = \varepsilon_s(i) E_s, \text{ for } \varepsilon_s(i) < \varepsilon_y$$

$$f_s(i) = f_s\left(1 + r\left(\frac{\varepsilon_s(i)}{\varepsilon_y} - 1\right)\right), \text{ for } \varepsilon_s(i) > \varepsilon_y$$

Layer force

$$T_s(i) = A_s(i) \cdot f_s(i)$$

Layer moment

$$M_s(i) = T_s(i)\left(d(i) - \frac{\beta c}{2}\right)$$

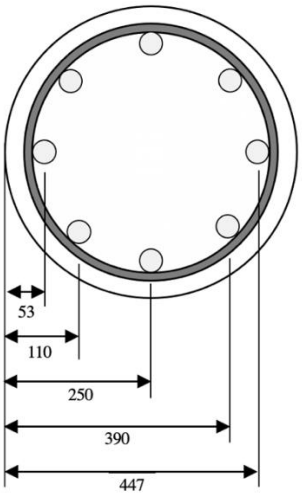

Figure A.1: Bar layout. Units in mm.

Table A.1: Summary of bar layer forces at the design rotation.

Layer	d(i) (mm)	N_b(i)	A_s(i) (mm^2)	$\Delta_s(i)$ (mm)	$\varepsilon_s(i)$	f_s(i) (MPa)	T_s(i) (kN)	M_s (kN-m)
1	53	1	169	-1.36	-0.0038	-381.44	-64	-1
2	110	2	337	0.29	0.0008	119.10	40	3
3	250	2	337	4.35	0.0121	391.25	132	27
4	390	2	337	8.41	0.0233	404.59	136	47
5	447	1	169	10.06	0.0279	410.02	69	28

Concrete Stress Block

Strain penetration length

$$l_{sp} = 0.022 f_y d_{b,e} = 0.134m$$

Plastic hinge length

$$L_p = 0.08H + l_{sp} = 0.302m$$

Yield curvature

$$\phi_y = \frac{2.25\varepsilon_y}{D} = 0.01155m^{-1}$$

Concrete compressive strain [8]

$$\varepsilon_c = \left[\frac{\theta H}{\left(H - \frac{L_p}{2}\right)L_p} + \phi_y\right] c = 0.0115$$

Concrete compressive strain corresponding to the peak unconfined compressive stress

$$\varepsilon_{co} = 0.0015 + \frac{f'_{ce}}{70000MPa} = 0.0022$$

Normalised concrete compressive strain

$$\frac{\varepsilon_c}{\varepsilon_{co}} = 5.13$$

Volumetric ratio of confinement hoops (10mm diameter bars at 50mm centres)

$$\rho_s = \frac{4A_{st}}{D' \cdot s} = 0.015$$

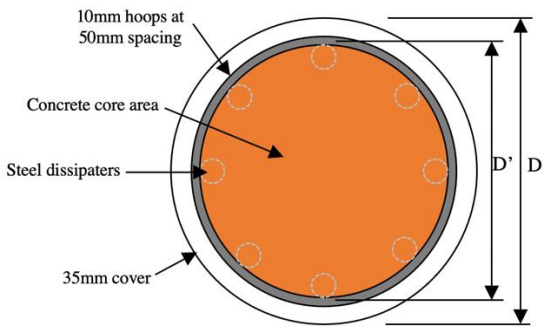

Figure A.2: Section at DCR joint.

Lateral pressure from lateral reinforcement

$$f_l = 0.5\rho_s f_{yh} = 3.74MPa$$

Ratio of area of longitudinal reinforcement (dissipaters) and area of concrete core

$$\rho_{cc} = \frac{8 \cdot 168.7mm^2}{138544mm^2} = 0.01$$

Confinement effectiveness coefficient for circular hoops, where s' is the clear spacing between hoops and D' is the distance to centre of hoop.

$$k_e = \frac{\left(1-\frac{s'}{2D'}\right)^2}{1-\rho_{cc}} = 0.92$$

Effective lateral confining stress

$$f'_l = 0.5k_e\rho_s f_{yh} = 3.43MPa$$

Confined concrete compressive strength

$$f'_{cc} = f'_c\left(-1.254 + 2.25\sqrt{1 + 7.94\frac{f'_l}{f'_c}}\right) - 2\frac{f'_l}{f'_c} = 72.59MPa$$

Ratio of the confined compressive strength and the unconfined compressive strength

$$\frac{f'_{cc}}{f'_c} = 1.40$$

For a concrete confinement ratio of 1.40 and a normalised concrete compressive strain of 5.13,

Stress block coefficient (magnitude)

$$\alpha = 1.344$$

Stress block coefficient (depth)

$$\beta = 0.878 \text{ (compared to 0.85 previously assumed)}$$

Concrete compression area

$$a = 2 \cdot acos\left(1 - \frac{c}{\frac{D}{2}}\right) = 1.85$$

$$A_c = \frac{1}{2}\left(\frac{D}{2}\right)^2 (a - \sin(a)) = 0.028m^2$$

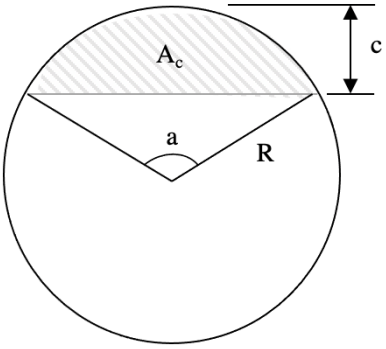

Figure A.3: Concrete stress block.

Concrete compression force (for circular section)

$$C_c = 0.9\alpha f'_c \beta A_c = 1544kN$$

Force Balance and Neutral Axis Iteration

Check the force balance

$$\sum F = N + T_{PT} + \sum T_s(i) - C_c = 270kN \neq 0$$

Iterate on the neutral axis depth (c) until the sum of the forces balances to zero.

Final neutral axis depth after iteration

$$c = 0.109m \text{ (22\% column diameter)}$$

Depth to concrete compressive block

$$\frac{a}{2} = \frac{\beta c}{2} = 0.0485m$$

Axial load

$$N = 210kN$$

Axial load moment contribution

$$M_N = N\left(\frac{D}{2} - \frac{a}{2}\right) = 42kN$$

Post-tensioning force

$$T_{PT} = 1267kN$$

Post-tensioning moment contribution

$$M_{PT} = T_{PT}\left(\frac{D}{2} - \frac{a}{2}\right) = 255kNm$$

Total bar force

$$\sum T_s\,(i) = 277kN$$

Bar moment contribution

$$M_s = \sum T_s(i)\left(d(i) - \frac{a}{2}\right) = 101kNm$$

Total moment capacity at design rotation

$$M_n = M_N + M_{PT} + M_S = 398kNm$$

Re-centring ratio

$$\lambda = \frac{M_{PT}+M_N}{2M_S} = 1.48$$

This is very close to the target re-centring ratio of 1.5

Part 2: DCR Response at the Decompression Point

Decompression moment

$$M_{dec} = \frac{T_{PT,i} + N}{A} \cdot Z = 69kNm$$

Base curvature

$$\phi_{col} = \frac{M_{dec}}{EI} = 0.002223m^{-1}$$

Rotation at the top of column

$$\theta_{col} = \frac{\phi_{col}H_c}{2} = 0.002335rad$$

Elastic deflection

$$\Delta_{dec} = \frac{2}{3}\theta_{col}H_c + \theta_{col}(H - H_c) = 0.003$$

Part 3: DCR Response at first Yield

The yield moment and displacement are first estimated to compute the elastic deflection under yield moment. The yield moment and yield displacement will be confirmed at the end of the design.

$$M_y = 302kNm$$

$$\Delta_y = 0.0204m$$

Base curvature

$$\phi_{col} = \frac{M_y}{EI_e} = 0.0097m^{-1}$$

Rotation at the top of column

$$\theta_{col} = \frac{\phi_{col} H_c}{2} = 0.01rad$$

Elastic deflection

$$\Delta_{e,y} = \frac{\phi_y H_c^2}{3} + \theta_{col}(H - H_c) = 0.0142m$$

Gap opening at yield

$$\theta_y = \frac{\Delta_y - \Delta_{e,y}}{H} = 0.00294rad$$

The neutral axis depth (c) is estimated and then later iterated until force balance is achieved.

$$c = 0.133m$$

Post-tensioning Bar Contribution

Tendon extension at design gap opening

$$\Delta_{PT} = n\theta_y\left(\frac{D}{2} - c\right) = 0.00034m$$

Additional post-tensioning load due to gap opening

$$\Delta T_{PT} = \frac{\Delta_{PT}}{l_{ub,PT}} E_{PT} A_{PT} = 31kN$$

Total post-tensioning force

$$T_{PT} = T_{PT,i} + \Delta T_{PT} = 931kN$$

Dissipating Bar Contribution

Table A.2: Summary of bar layer forces at yield.

Layer	d(i)	N_b(i)	A_s(i) (mm^2)	$\Delta_s(i)$ (mm)	$\varepsilon_s(i)$	f_s(i) (MPa)	T_s(i) (kN)	M_s (kN-m)
1	53	1	169	-0.23	-0.0007	-96.30	-16	-0.08
2	110	2	337	-0.07	-0.0002	-27.47	-9	-0.57
3	250	2	337	0.34	0.0010	141.59	48	10
4	390	2	337	0.76	0.0021	310.65	105	36
5	447	1	169	0.92	0.0026	379.48	64	26

Total bar force

$$\sum T_s(i) = A_s(i) \cdot f_s(i) = 191kN$$

Maximum bar strain (from Table A.2)

$$\varepsilon_{s,max} = 0.0026$$

Concrete Compressive Block

Concrete compressive strain [8]

$$\varepsilon_c = \left[\frac{\theta_y H}{\left(H - \frac{L_p}{2}\right)L_p} + \phi_y\right] c = 0.0029$$

Normalised concrete compressive strain

$$\frac{\varepsilon_c}{\varepsilon_{co}} = 1.3$$

For a concrete confinement ratio of 1.4 and a normalised concrete compressive strain of 1.3,

Stress block coefficient (magnitude)

$$\alpha = 0.943$$

Stress block coefficient (depth)

$$\beta = 0.722$$

Concrete compression area

$$a = 2 \cdot acos\left(1 - \frac{c}{\frac{D}{2}}\right) = 2.17$$

$$A_c = \frac{1}{2}\left(\frac{D}{2}\right)^2 (a - \sin(a)) = 0.042m^2$$

Concrete compression force

$$C_c = 0.9\alpha f'_c \beta A_c = 1332kN$$

Balance of Forces and Neutral Axis Iteration

$$\sum F = N + T_{PT} + \sum T_s(i) - C_c = 0kN$$

Iterate on the neutral axis depth (c) until the sum of the forces balances to zero. Additionally, update the yield displacement and yield moment with each iteration step.

$$\Delta_y(i+1) = \frac{\varepsilon_y}{\varepsilon_{s,max}}\left(\Delta_y(i) - \Delta_e\right) + \Delta_e$$

Depth to concrete compressive block

$$\frac{a}{2} = \frac{\beta c}{2} = 0.048m$$

Axial load moment contribution

$$M_N = N\left(\frac{D}{2} - \frac{a}{2}\right) = 42kN$$

Post-tensioning moment contribution

$$M_{PT} = T_{PT}\left(\frac{D}{2} - \frac{a}{2}\right) = 188kNm$$

Bar moment contribution

$$M_s = \sum T_s(i)\left(d(i) - \frac{\beta c}{2}\right) = 70kNm$$

Yield moment

$$M_y = M_N + M_{PT} + M_S = 301kNm$$

Re-centring ratio

$$\lambda = \frac{M_{PT}+M_N}{2M_S} = 1.64$$

Step 4: DCR Response at the Ultimate Displacement Demand (MCE-Level Seismic Event)

The ultimate displacement demand (Δ_u) is taken as the displacement at a Maximum Considered Earthquake (MCE) which is 1.5 times the design displacement (Δ_d).

$$\Delta_u = 1.5\Delta_d = 0.102m$$

Similar at yield, the ultimate moment is estimated to compute the elastic deflection. The ultimate moment will be confirmed at the end of the design.

$$M_u = 415kNm$$

Base curvature

$$\phi_{col} = \frac{M_u}{EI_e} = 0.0133m^{-1}$$

Rotation at the top of column

$$\theta_{col} = \frac{\phi_{col} H_c}{2} = 0.014rad$$

Elastic deflection

$$\Delta_{e,u} = \frac{\phi_y H_c^2}{3} + \theta_{col}(H - H_c) = 0.0196m$$

Gap opening at MCE

$$\theta_u = \frac{\Delta_u - \Delta_{e,u}}{H} = 0.039rad$$

The neutral axis depth (c) is initially estimated and then later iterated on until force balance is achieved.

$$c = 0.113m$$

Post-tensioning Bar Contribution

Tendon extension at design gap opening

$$\Delta_{PT} = n\theta_u\left(\frac{D}{2} - c\right) = 0.00541m$$

Additional post-tensioning load due to gap opening

$$\Delta T_{PT} = \frac{\Delta_{PT}}{l_{ub,PT}} E_{PT} A_{PT} = 486kN$$

Total post-tensioning force

$$T_{PT} = T_{PT,i} + \Delta T_{PT} = 1386kN$$

Dissipating Bar Contribution

Table A.3: Summary of bar layer forces at MCE.

Layer	d(i)	N_b(i)	A_s(i) (mm^2)	$\Delta_s(i)$ (mm)	$\varepsilon_s(i)$	f_s(i) (MPa)	T_s(i) (kN)	M_s (kN-m)
1	53	1	169	-2.36	-0.0065	-369.21	-62	0
2	110	2	337	-0.11	-0.0003	-44.78	-15	-1
3	250	2	337	5.41	0.0150	394.76	133	26
4	390	2	337	10.93	0.0304	412.92	139	47
5	447	1	169	13.18	0.0366	420.31	71	28

Total bar force

$$\sum T_s(i) = A_s(i) \cdot f_s(i) = 100kN$$

Maximum bar strain (from Table A.3)

$$\varepsilon_{s,max} = 0.0366$$

Concrete Compressive Block

Concrete compressive strain [8]

$$\varepsilon_c = \left[\frac{\theta_y H}{\left(H - \frac{Lp}{2}\right)L_p} + \phi_y\right] c = 0.0172$$

Normalised concrete compressive strain

$$\frac{\varepsilon_c}{\varepsilon_{co}} = 7.66$$

For a concrete confinement ratio of 1.4 and a normalised concrete compressive strain of 7.66,

Stress block coefficient (magnitude)

$$\alpha = 1.277$$

Stress block coefficient (depth)

$$\beta = 0.939$$

Concrete compression area

$$a = 2 \cdot acos\left(1 - \frac{c}{\frac{D}{2}}\right) = 1.98$$

$$A_c = \frac{1}{2}\left(\frac{D}{2}\right)^2 (a - \sin(a)) = 0.033m^2$$

Concrete compression force

$$C_c = 0.9\alpha f'_c \beta A_c = 1862kN$$

Balance of Forces and Neutral Axis Iteration

$$\sum F = N + T_{PT} + \sum T_s(i) - C_c = 0kN$$

Iterate on the neutral axis depth (c) and ultimate moment until a force balance is achieved.

Depth to concrete compressive block

$$\frac{a}{2} = \frac{\beta c}{2} = 0.053m$$

Axial load moment contribution

$$M_N = N\left(\frac{D}{2} - \frac{a}{2}\right) = 42kN$$

Post-tensioning moment contribution

$$M_{PT} = T_{PT}\left(\frac{D}{2} - \frac{a}{2}\right) = 273kNm$$

Bar moment contribution

$$M_s = \sum T_s(i)\left(d(i) - \frac{\beta c}{2}\right) = 100kNm$$

Ultimate moment

$$M_u = M_N + M_{PT} + M_S = 415kNm$$

Re-centring ratio

$$\lambda = \frac{M_{PT} + M_N}{2M_S} = 1.57$$

Part 5: Summary

Table A.4: Summary of monotonic response contributions.

	Gap opening, θ (rad)	**M_N (kN-m)**	**M_{PT} (kN-m)**	**M_S (kN-m)**	**M_u (kN-m)**
Decompression	0.0	13	56	0	0
Yield	0.00294	42	188	0	69
Design	0.029	42	255	70	301
Ultimate (MCE)	0.039	42	273	101	398

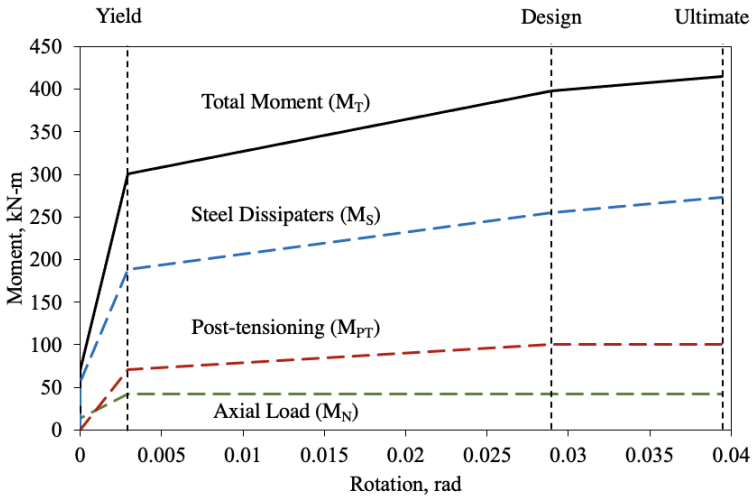

Figure A.4: Backbone moment-rotation response.